NANO LETTERS

pubs.acs.org/NanoLett Letter

Optical Encryption in the Photonic Orbital Angular Momentum Dimension via Direct-Laser-Writing 3D Chiral Metahelices

Shunli Liu,† Xinghao Wang,† Jincheng Ni, Yang Cao, Jiawen Li,* Chaowei Wang, Yanlei Hu, Jiaru Chu, and Dong Wu*

Cite This: *Nano Lett.* 2023, 23, 2304−2311 Read Online

ACCESS | Metrics & More | Article Recommendations | Supporting Information

ABSTRACT: Vortex beams, which intrinsically possess optical orbital angular momentum (OAM), are considered as one of the promising chiral light waves for classical optical communications and quantum information processing. For a long time, it has been an expectation to utilize artificial three-dimensional (3D) chiral metamaterials to manipulate the transmission of vortex beams for practical optical display applications. Here, we demonstrate the concept of selective transmission management of vortex beams with opposite OAM modes assisted by the designed 3D chiral metahelices. Utilizing the integrated array of the metahelices, a series of optical operations, including display, hiding, and even encryption, can be realized by the parallel processing of multiple vortex beams. The results open up an intriguing route for metamaterial-dominated optical OAM processing, which fosters the development of photonic angular momentum engineering and high-security optical encryption.

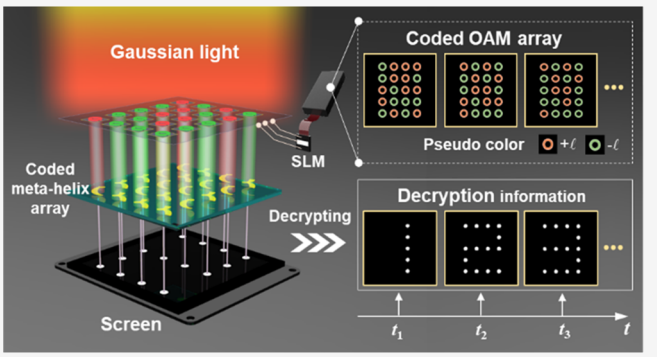

KEYWORDS: *direct laser writing, chiral metahelix, vortex beam, orbital angular momentum, optical encryption*

Light waves with chiral characteristics intrinsically possess optical angular momentum such as spin angular momentum (SAM) carried by circularly polarized light and orbital angular momentum (OAM) carried by vortex beams.[1] Distinguished with the locally polarization-related SAM with only the binary helicity index ($+\sigma$, $-\sigma$), the photonic OAM manifests a spatially twisted wavefront of $e^{il\varphi}$, where φ is the azimuthal angle, and l is the OAM mode index. Emerging as a new photonic dimension, the photonic OAM has been widely applied in fundamental research of chiral light−matter interactions[2−5] and practical applications including optical tweezers,[6−8] high-bandwidth optical communications,[9−11] multiplexed holography,[12−14] chiral structure processing,[15−18] and integrated nanophotonic devices.[19−22] Analogous to the conventional physical dimensions of light, such as amplitude,[23] frequency,[24] polarization,[25] and lifetime,[26] photonic OAM can also be exploited as an orthogonal information channel in modern optical information technologies. As such, functional metadevices capable of OAM processing are essential for the next-generation optical communication system.

In this context, some two-dimensional (2D) metasurface, such as Dammann gratings,[27,28] plasmonic nanoring apertures,[29−31] plasmonic nanogratings,[32−35] and integrated metadevices,[36−39] have been used for OAM beam generation, free-space OAM multiplexing, on-chip OAM multiplexing, and OAM mode detecting, respectively. Compared with these 2D metadevices, three-dimensional (3D) optical metamaterials theoretically have greater potential to manipulate light waves due to their z-direction geometric degrees of freedom for enhancing light−matter interactions. For instance, 3D optical metamaterials have demonstrated a powerful performance in manipulating various properties of light, mainly including frequency[40−43] and polarization.[44−46] Typically, through the elaborate 3D metamaterial design, light waves of specific frequencies or polarizations can pass through or be forbidden as expected, which has facilitated the paradigm of tailoring optical responses with metamaterials. On the basis of these studies, 3D metamaterials are naturally regarded as an ideal platform for manipulating photonic OAM and have long been pursued. It has been reported that some 3D metamaterials, such as a chiral dipolar scatterer,[47] stereostructures,[3] and nanoparticle aggregates,[48,49] can respond to opposite photonic OAM modes for yielding chiroptical phenomena. Despite these impressive advances, OAM-dependent practical optical

Received: December 29, 2022
Revised: February 21, 2023
Published: March 7, 2023

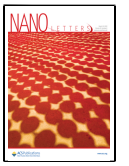

https://doi.org/10.1021/acs.nanolett.2c04860
Nano Lett. 2023, 23, 2304−2311

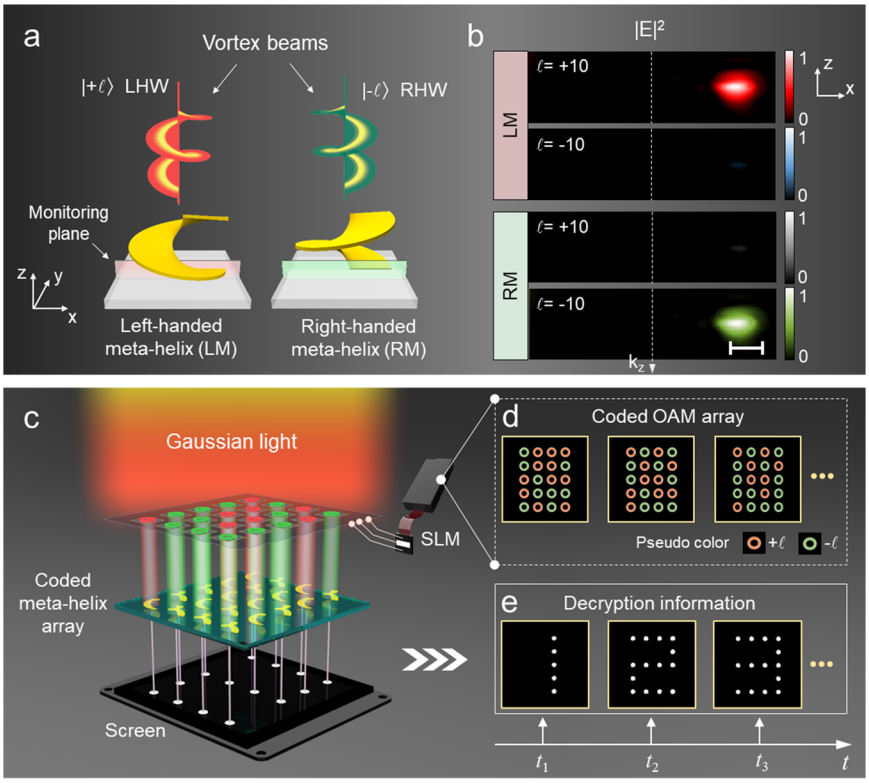

Figure 1. Principle of optical encryption utilizing vortex beams and chiral metahelices. (a) Illustration of the opposite vortex beams ($+l$, $-l$) illuminating on the opposite 3D chiral metahelices at normal incidence. LHW/RHW, left-/right-handed helical wavefront; LM/RM, left-/right-handed metahelix. (b) Optical intensity distribution of varying OAM−metahelix combinations in the monitoring planes. The light spots all appear on the right side of the optical axis k_z, corresponding to the starting side of the chiral metahelices. The images are presented in pseudocolors. Simulation area: monitoring planes in panel a. Scale bars, 1 μm. (c) Concept of optical encryption on the coded metahelix array. (d) The information sent on time is encoded into a specific coded OAM array by the SLM. (e) The receiver can obtain the decryption information using the coded metahelix array.

encryption applications via 3D metamaterials have remained an ongoing challenge.

Here, we experimentally demonstrate the selective transmission management of vortex beams with opposite OAM modes through designed 3D chiral metahelices. The staircase-like chiral metahelices, which are fabricated by femtosecond direct laser writing, can selectively display or hide the incident vortex beams with high contrast. Furthermore, multiple vortex beams for optical image operations of display, hiding, and encryption can be flexibly implemented on the integrated array of chiral metahelices. Our work opens new horizons for optical communication applications in the light's OAM dimension and could thereby advance the development of miniaturized components in integrated photonics.

The optical encryption principle is illustrated in Figure 1. For a pair of opposite vortex beams, they possess opposite helical wavefronts and OAM mode indices ($+l$, $-l$) (hereinafter referred as the OAM mode for simplicity), as shown in the top of Figure 1a. However, they manifest identical donut-shaped optical intensity distributions and nonselective transmission behavior in homogeneous materials, which is generally considered difficult to be broken by metamaterials. Here, the intrinsic OAM modes of vortex beams with a left- and right-handed helical wavefront are denoted as positive ($+l$) and negative ($-l$), respectively. Then, we designed a 3D chiral metahelix in analogue of spiral staircases (bottom in Figure 1a) as the basic optical elements to break the transmission symmetry of the opposite vortex beams. The 3D left-/right-handed metahelix (LM/RM) was designed according to Figure S1, which can engender selective transmission behaviors to vortex beams in subsequent simulations and experiments.

To verify our selective transmission statement, the xz-plane optical intensity distribution with varying OAM−metahelix combinations was simulated based on the commercial finite-difference time-domain (FDTD) algorithm (Figure 1b, presented in pseudocolors; see Section S1 for more details). The simulation area is the monitoring plane with a size of 8 × 2.3 μm in Figure 1a. Unlike the local SAM properties of circularly polarized light, the OAM properties of vortex beams are spatially distributed and closely related to the beam diameter. Therefore, for effectively coupling the spatial photonic OAM characteristics, the lateral diameter and helical pitch H of the chiral metahelix are set to D = 6 μm and H = 6 μm considering both simulation results and experimental fabrication. Besides, the wavelength of vortex beams is set to 800 nm, which is commonly used in the laboratory. In this case, the most obvious selective transmission can be observed when the incident OAM modes are $l = \pm 10$ (Figure S2). In terms of the LM, it is a "green channel" for the OAM mode of l = +10, accompanied by a bright spot in the simulation area. On the contrary, the vortex beam of $l = -10$ is almost completely blocked. Compared with the LM, the phenomena are reversed on the RM, manifesting that the OAM mode of l = +10 will be blocked, while $l = -10$ can pass. It is worth noting that all the bright spots appear on the right side of the central optical axis k_z, corresponding to the starting position of the chiral

https://doi.org/10.1021/acs.nanolett.2c04860
Nano Lett. 2023, 23, 2304−2311

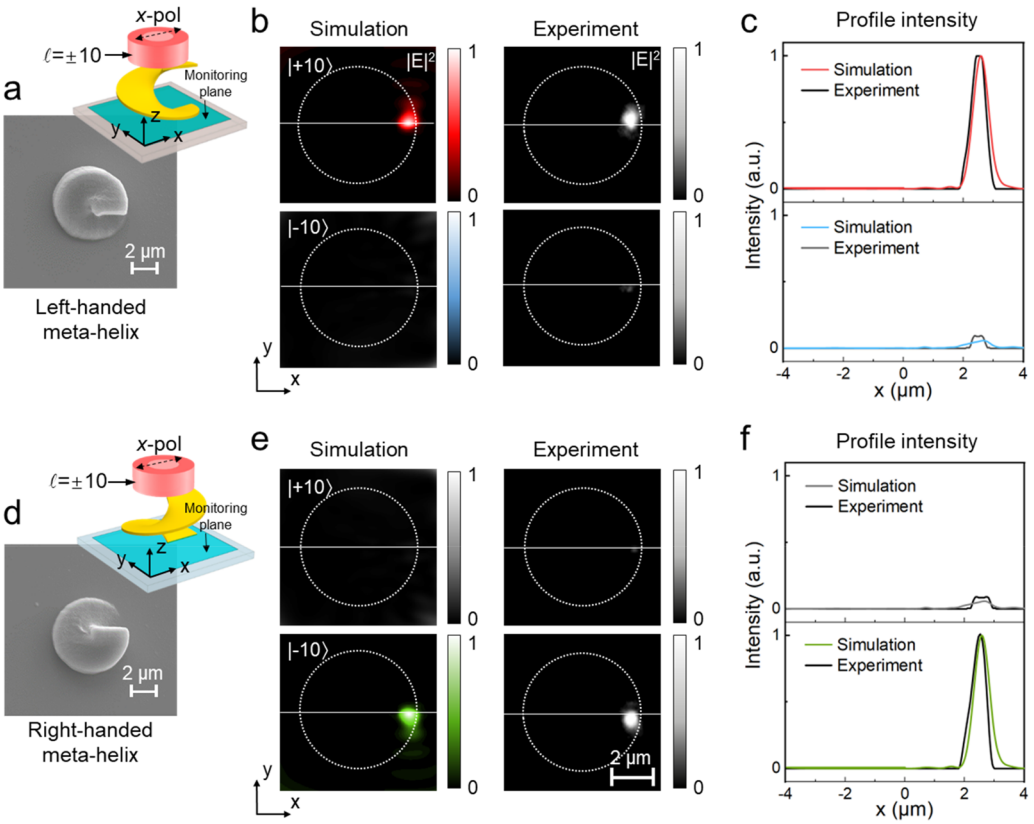

Figure 2. Distinctive OAM mode selectivity of opposite 3D chiral metahelices. (a) SEM images of fabricated LM. The inset shows a schematic diagram of the interaction between opposite vortex beams (l = ±10) and LM. Simulation area: the blue planes. (b) Simulated and experimental optical intensity distributions of the LM illuminated by the vortex beams with opposite OAM modes in the monitoring plane. Dashed white lines indicate the geometric profile of metahelices. (c) Experimental and simulated amplitude modulus distributions in panel b, as labeled by the solid white lines. (d–f) Same as panels a–c, corresponding to the RM.

metahelix. In addition, the OAM mode l with selective transmission properties is not fixed and can be controlled by the lateral diameter D of the chiral metahelices (Figure S3).

Furthermore, by simultaneously integrating vortex beams and chiral metahelices, optical encryption can be executed through the many-to-many parallel processing strategy. As demonstrated in Figure 1c, the incident Gaussian light can be modulated into varying coded OAM arrays of 5 units × 4 units by a liquid-crystal spatial light modulator (SLM). On one hand, these coded OAM arrays sent on time have identical extrinsic optical intensity distributions, which can protect the information from being stolen by potential listeners (Figure 1d). On the other hand, even if the OAM arrangement in the array is deciphered, it is still impossible to know the valid information it carries. To decrypt the valid information, it is necessary to use a coded metahelix array arranged in accordance with the agreement, wherein the units are separated by a spacing that is larger than the diffraction–interference distance of the adjacent vortex beams, allowing for the parallel manipulation of multiple vortex beams without crosstalk. With the assistance of the coded metahelix array, the receiver can obtain the decryption information in time at the terminal of the optical communication system, as shown in Figure 1e.

To further verify the OAM selectivity of chiral metahelices, the process of the light–matter interaction was analyzed here. In the experiment, the chiral metahelices were fabricated in polymer resist SZ2080 by femtosecond direct laser writing (see Section S1 for more details). The scanning electron microscope (SEM) images of fabricated LM and RM with the same parameters as the simulation are shown in Figure 2a,d, respectively. For avoiding the interference of photonic SAM, the incident vortex beams were adjusted to be linearly polarized along the x-direction in this paper.[47] In the simulation, x-direction linearly polarized vortex beams can be directly created according to eq 1:

$$E^{\text{in}}(r, \varphi) = C\frac{r^{|l|}}{\sqrt{|l|!}}\exp\left(-\frac{r^2}{w_0^2}\right)\exp(il\varphi)\hat{x} \quad (1)$$

where C is a normalized constant independent of the OAM mode l and the polar diameter r, w_0 is the beam waist consistent with the experimental conditions, and $\hat{x}$ refers to the polarization direction of the vortex beams. In the experiment (using the optical system shown in Figure S4), x-polarized fundamental-mode Gaussian light was collimated to illuminate a fork hologram loaded on the SLM for yielding the vortex beam at a wavelength of 800 nm. The well-prepared vortex beam was finally focused on the sample by a high-numerical-aperture objective, and its intensity profile and phase distribution can be analyzed by vectorial Debye diffraction theory (Figure S5).

Before interacting with the chiral metahelix, the opposite vortex beams (l = ±10) have identical optical intensity distributions both in simulation and experiment (Figure S6). However, this symmetry will be broken by the chiral metahelix. The top right corners of Figure 2a,d show the schematics of the vortex beams illuminating the chiral metahelices at normal

https://doi.org/10.1021/acs.nanolett.2c04860
Nano Lett. 2023, 23, 2304–2311

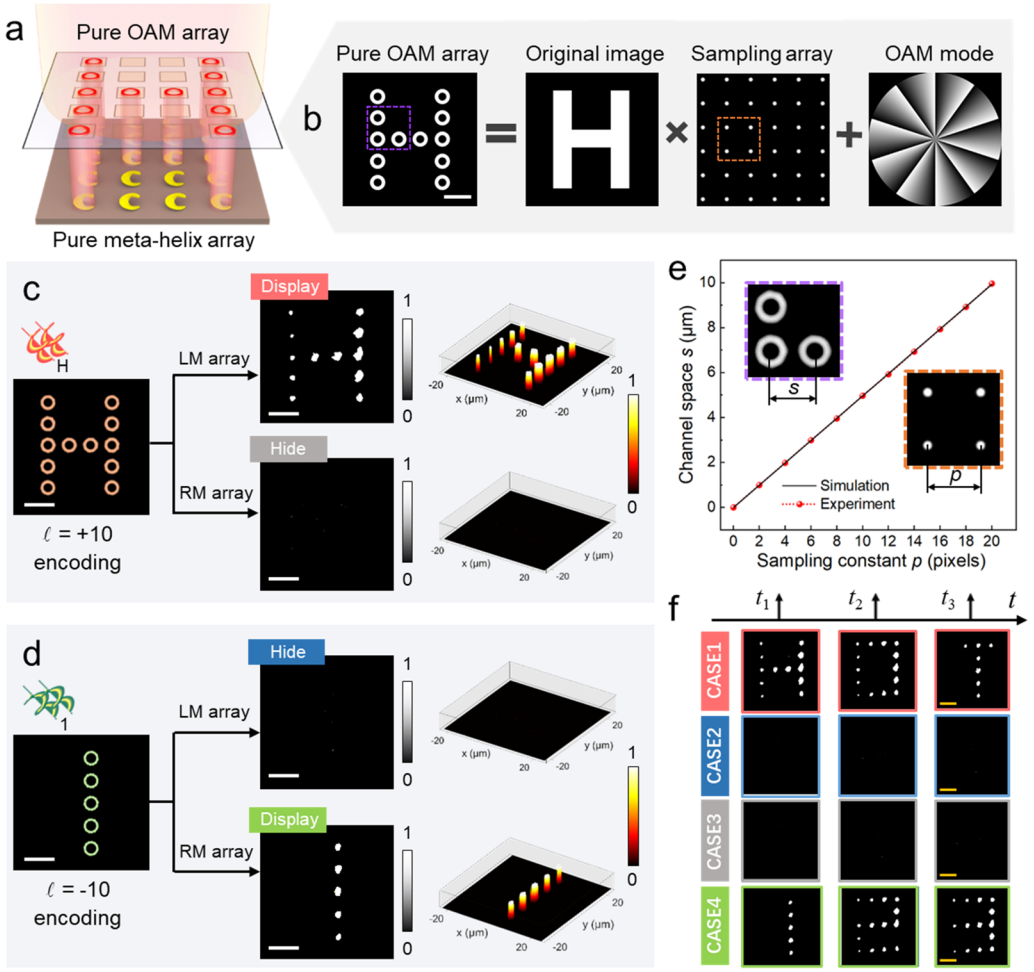

Figure 3. Optical display/hiding of OAM-preserved images on LM/RM arrays. (a) Schematic of selective optical display/hiding of a pure OAM array on a pure metahelix array. (b) Design principle of a pure OAM array for the given original image "H". (c, d) Pattern "H" encoded by $l = +10$ (c) and pattern "1" encoded by $l = -10$ (d) are processed by the opposite chiral metahelix arrays. (e) Relationship between the channel space s and the sampling constant p. (f) Experiment of time-division multiplexed processing retrieved from the four OAM−metahelix cases at three different moments. Scale bars, 10 μm.

incidence, wherein we focus our attention on the blue monitoring planes. The monitoring planes are square windows of 8 × 8 μm located at the bottom of the metahelix, which is also the observation plane in the experiment. The simulated and experimental optical light distributions $|E|^2$ for varying OAM−metahelix combinations are demonstrated in Figure 2b,e. In the monitoring plane of LM, there will be a clearly visible spot for the OAM mode of $l = +10$, while the light almost disappears for $l = -10$. However, for the RM, the phenomena are reversed compared with the LM. It is worth mentioning that the metahelix is insensitive to the polarization state of the incident vortex beams, as shown in Figure S7.

It is worth noting that the light spots in Figure 2b,e have an equal offset relative to the optical axis, which appears at the bottom starting side of the chiral metahelices and has little effect on the subsequent optical applications. Besides, the optical intensity at the solid white lines in Figure 2b,e is also recorded, indicating that the experimental results are in good agreement with the simulated analysis (as shown in Figure 2c,f). Besides, the phenomenon of selective transmission management of vortex beams can be observed in both reflection and transmission experiments, but the selective modes of vortex beams in the reflection and transmission are opposite. More importantly, the chiral metahelices also exhibit good performance in a broadband range from 580 nm to 1100 nm (Figures S8 and S9), which lays the foundation for wavelength-multiplexed optical applications.

Integrated chiral metahelix arrays enable the parallel transmission manipulation of multiple vortex beams, opening up the possibilities of metahelix-dominated optical image processing. For the most general case, selective optical display/hiding can be achieved by processing a pure OAM array with a pure chiral metahelix array, as shown in Figure 3a. The multifoci pure OAM array is designed according to the principle in Figure 3b (more details in Figure S10). As a demonstration, we perform a convolution operation on the original image "H" by the sampling array (equivalent to a 2D Dirac comb function) with a sampling constant of p. Then, the weighted Gerchberg−Saxton (GS) algorithm is adopted to calculate the sampling hologram. By adding a helical phase plate to the sampling hologram, we finally obtain an OAM-preserved hologram that can be reconstructed into a pure OAM array of "H" with desired OAM mode. In addition, pure OAM arrays of other preset images can be generated by the above steps (Figure S10).

https://doi.org/10.1021/acs.nanolett.2c04860
Nano Lett. 2023, 23, 2304−2311

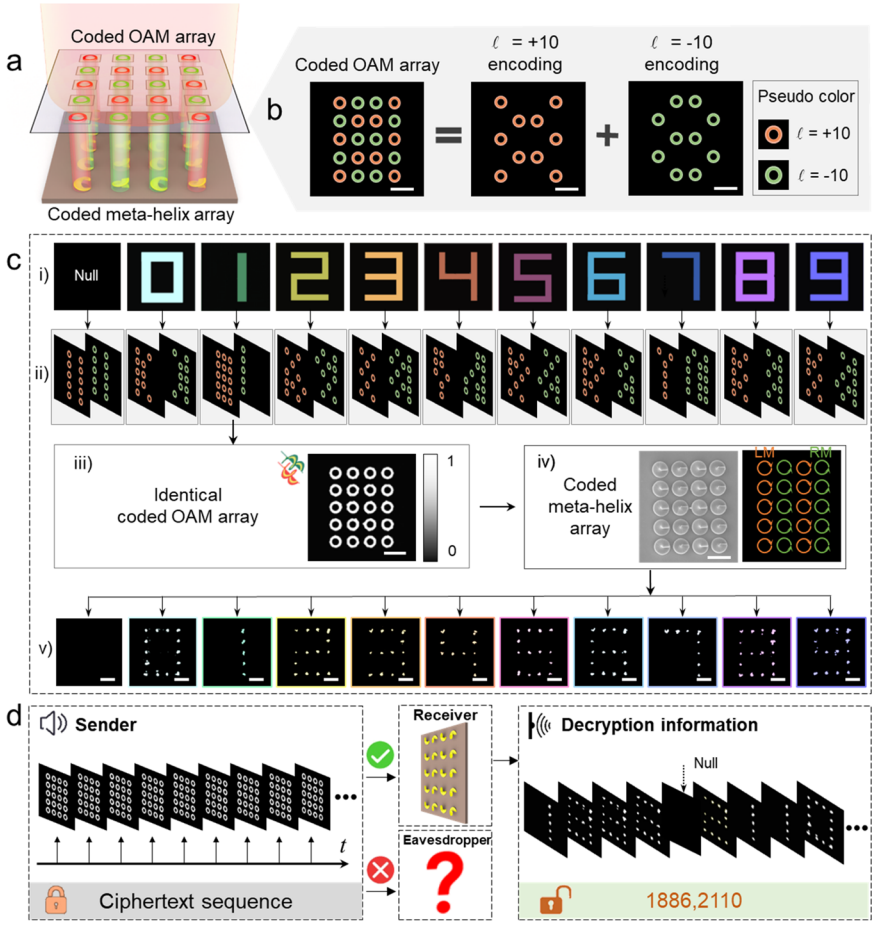

Figure 4. Experimental demonstration of using a coded metahelix array for optical encryption. (a) Principle of optical encryption by coded OAM array and coded metahelix array. (b) Schematic of synthesizing a coded OAM array from two pure OAM arrays. (c) OAM encryption and decryption for varying images. All images i) have the identical synthetic coded OAM array iii) and differentiated decrypted information v). (d) The OAM sequence sent in chronological order can prevent eavesdroppers and be received by the holder of the coded metahelix array. Scale bars, 10 μm.

For a specific OAM mode of the vortex beam array, it will yield different results on varying pure metahelix arrays (also using the platform in Figure S4). For example, the multifoci "H" pattern encoded by the OAM mode of $l = +10$ is displayed on the LM array but hidden on the RM array (Figure 3c), whereas for the multifoci pattern "1" encoded by $l = -10$, it vanishes on the LM array but appears on the RM array (Figure 3c). From the optical intensity histograms, it can be found that all four varying OAM−metahelix combinations show the robustness of display/hiding effects, and the intensity difference between pixels is mainly caused by the alignment errors of vortex beams and chiral metahelices.

In the implementation of the pure OAM array, the channel spacing s is linearly related to the sampling constant p (Figure 3e) and can be described as follows

$$s = \frac{\lambda f_1}{d_{\text{pixel}} N_{\text{pixel}}} \times \frac{f_{\text{objective}}}{f_2} \times p \tag{2}$$

where $\lambda = 800$ nm is the wavelength of light source, $f_1 = 600$ mm and $f_2 = 200$ mm are the focal lengths of convex lens 1 and convex lens 2, $d_{\text{pixel}} = 8$ μm and $N_{\text{pixel}} = 1080$ are the pixel pitch and pixels number on the SLM panel, and $f_{\text{objective}} = 1.8$ mm is the focal length of the objective lens in Figure S4. To avoid crosstalk in pure OAM arrays, the sampling constant is set to $p = 16$ pixels for the selected OAM modes of $l = \pm 10$, and the channel spacing calculated according to the eq 2 is $s = 8$ μm.

Benefiting from the fast response speed of the hologram-loaded SLM in Figure S4, it opens the possibility of achieving time-division multiplexing for dynamic optical display/hiding. Figure 3f illustrates the experimental time-division images of four OAM−metahelix cases at three different moments (t_1, t_2, and t_3), in which the time interval between two adjacent moments could theoretically be as short as the response time of the SLM. Furthermore, owing to the broadband properties of chiral metahelices, wavelength also holds great promise to be added as another degree of freedom to realize higher-dimensional selective OAM processing techniques.

Furthermore, the chiral metahelix can display a specific OAM mode while hiding the opposite one, which inspires the application of optical information encryption with a high level of security, as shown in Figure 4a. For the implementation of optical encryption, we first designed a coded chiral metahelix array according to the encryption protocol. Here, we employed a design in which left- and right-handed metahelices were alternately arranged column by column (iv in Figure 4c). Correspondingly, the coded OAM array is no longer composed of a pure OAM mode but contains two parts: positive information ($+l$ encoding) and negative information ($-l$

https://doi.org/10.1021/acs.nanolett.2c04860
Nano Lett. 2023, 23, 2304−2311

encoding), as shown in Figure 4b. The detailed generation process of the coded OAM arrays is shown in Figure S11.

More generally, the OAM-coded method can be utilized for encoding varying original images such as "Null" and ten Arabic numerals from 0 to 9 (Figure 4c), yielding 11 coded OAM arrays. In terms of all original images (i in Figure 4c), they have identical synthetic OAM-encrypted arrays, whose information cannot be deciphered by direct observation. However, the coded metahelix array can act as a key to filter out the redundant interference in the coded OAM array. As such, those identically coded OAM arrays serving as ciphertext in the optical communications can be reconstructed into varying decrypted information by the coded metahelix array, as shown in the bottom v) of Figure 4c.

Then, using the OAM-coded ciphertext sequences and coded metahelix array, we demonstrated a high-security scheme for all-optical information transmission (Figure 4d). At first, the OAM ciphertext sequence designed by the sender is sent frame by frame in chronological order. For eavesdroppers, they can only get the indistinguishable ciphertext sequences, even if they can intercept the signal, while the valid information can be obtained by the holder of a coded metahelix array. Moreover, "Null" is employed as a delimiter for the sentence segmentation. As such, the OAM ciphertext sequence is successfully decrypted into a meaningful plaintext message of "1886, 2110". The proposed concept of high-security information encryption might be interesting, from both fundamental and application points of view, to extend the OAM-enabled encryption into the optical communications regime.

In summary, we have demonstrated a novel concept for selective transmission management of opposite vortex beams using 3D staircase-like chiral metahelices. By simultaneously integrating vortex beams and chiral metahelices, an optical display or hiding that relies on parallel OAM processing can be executed. As a proof-of-concept demonstration, we also demonstrate decrypting OAM-encrypted images using a coded chiral metahelix array as a key. Notably, in addition to orbital angular momentum and time dimension, the broadband performance of the chiral metahelix makes wavelength division multiplexing a potential possibility, which greatly expands the degrees of freedom of metahelix-based optical encryption. Due to the restriction of the imaging range of the charge-coupled device (CCD) in the experiment, we only show a limited pixel array of 5 × 4 in the work. In the future, the chiral metahelices can be integrated with OAM generators[36,38,39,50,51] on a large scale to simplify the optical system and reduce costs, and thus hold great promise in information display, image encryption, data storage, and optical communications.

■ ASSOCIATED CONTENT

Supporting Information

The Supporting Information is available free of charge at https://pubs.acs.org/doi/10.1021/acs.nanolett.2c04860.

Materials and methods; design principles of 3D chiral metahelices; numerical simulation of a left-handed metahelix; relationship between the lateral diameter D and OAM mode l; optical platform; amplitude and phase distributions of an optical vortex; simulated and experimental focus profile; simulated optical intensity distributions with different polarization states; simulated reflectivity over a wide wavelength range; broadband properties of chiral metahelices; design process of OAM-array holograms; and detailed principles of an OAM-encrypted dynamic hologram (PDF)

■ AUTHOR INFORMATION

Corresponding Authors

Jiawen Li − *Hefei National Laboratory for Physical Sciences at the Microscale, Key Laboratory of Precision Scientific Instrumentation of Anhui Higher Education Institutes, CAS Key Laboratory of Mechanical Behavior and Design of Materials, Department of Precision Machinery and Precision Instrumentation, University of Science and Technology of China, Hefei 230026, China;* orcid.org/0000-0003-3950-6212; Email: jwl@ustc.edu.cn

Dong Wu − *Hefei National Laboratory for Physical Sciences at the Microscale, Key Laboratory of Precision Scientific Instrumentation of Anhui Higher Education Institutes, CAS Key Laboratory of Mechanical Behavior and Design of Materials, Department of Precision Machinery and Precision Instrumentation, University of Science and Technology of China, Hefei 230026, China;* orcid.org/0000-0003-0623-1515; Email: dongwu@ustc.edu.cn

Authors

Shunli Liu − *Hefei National Laboratory for Physical Sciences at the Microscale, Key Laboratory of Precision Scientific Instrumentation of Anhui Higher Education Institutes, CAS Key Laboratory of Mechanical Behavior and Design of Materials, Department of Precision Machinery and Precision Instrumentation, University of Science and Technology of China, Hefei 230026, China*

Xinghao Wang − *Hefei National Laboratory for Physical Sciences at the Microscale, Key Laboratory of Precision Scientific Instrumentation of Anhui Higher Education Institutes, CAS Key Laboratory of Mechanical Behavior and Design of Materials, Department of Precision Machinery and Precision Instrumentation, University of Science and Technology of China, Hefei 230026, China*

Jincheng Ni − *Hefei National Laboratory for Physical Sciences at the Microscale, Key Laboratory of Precision Scientific Instrumentation of Anhui Higher Education Institutes, CAS Key Laboratory of Mechanical Behavior and Design of Materials, Department of Precision Machinery and Precision Instrumentation, University of Science and Technology of China, Hefei 230026, China*

Yang Cao − *Hefei National Laboratory for Physical Sciences at the Microscale, Key Laboratory of Precision Scientific Instrumentation of Anhui Higher Education Institutes, CAS Key Laboratory of Mechanical Behavior and Design of Materials, Department of Precision Machinery and Precision Instrumentation, University of Science and Technology of China, Hefei 230026, China*

Chaowei Wang − *Hefei National Laboratory for Physical Sciences at the Microscale, Key Laboratory of Precision Scientific Instrumentation of Anhui Higher Education Institutes, CAS Key Laboratory of Mechanical Behavior and Design of Materials, Department of Precision Machinery and Precision Instrumentation, University of Science and Technology of China, Hefei 230026, China*

Yanlei Hu − *Hefei National Laboratory for Physical Sciences at the Microscale, Key Laboratory of Precision Scientific Instrumentation of Anhui Higher Education Institutes, CAS Key Laboratory of Mechanical Behavior and Design of*

https://doi.org/10.1021/acs.nanolett.2c04860
Nano Lett. 2023, 23, 2304−2311

Materials, Department of Precision Machinery and Precision Instrumentation, University of Science and Technology of China, Hefei 230026, China; orcid.org/0000-0003-1964-0043

Jiaru Chu − *Hefei National Laboratory for Physical Sciences at the Microscale, Key Laboratory of Precision Scientific Instrumentation of Anhui Higher Education Institutes, CAS Key Laboratory of Mechanical Behavior and Design of Materials, Department of Precision Machinery and Precision Instrumentation, University of Science and Technology of China, Hefei 230026, China;* orcid.org/0000-0001-6472-8103

Complete contact information is available at: https://pubs.acs.org/10.1021/acs.nanolett.2c04860

Author Contributions

†S.L. and X.W. contributed equally to this work. S.L., X.W., and D.W. proposed the idea and conceived the experiment. S.L., X.W., Y.C., C.W., and J.L. performed the experiments. S.L. and J.N. performed the numerical simulations. S.L. and X.W. wrote the manuscript. J.N., J.L., Y.H., D.W., and J.C. reviewed and revised the manuscript.

Notes

The authors declare no competing financial interest.

■ ACKNOWLEDGMENTS

This work was supported by the National Natural Science Foundation of China (Nos. 61927814, 52122511, 52075516, and 62005262), the Open Project of Wuhan National Laboratory for Optoelectronics (No. 2019WNLOKF014), CAS Project for Young Scientists in Basic Research (Grant No.YSBR-049), and the Fundamental Research Funds for the Central Universities (WK5290000003). We acknowledge the Experimental Center of Engineering and Material Sciences at USTC for the fabrication and measuring of samples. This work was partly carried out at the USTC Center for Micro and Nanoscale Research and Fabrication.

■ REFERENCES

(1) Franke-Arnold, S.; Allen, L.; Padgett, M. Advances in Optical Angular Momentum. *Laser Photonics Review* **2008**, *2*, 299−313.

(2) Zambrana-Puyalto, X.; Vidal, X.; Molina-Terriza, G. Angular Momentum-Induced Circular Dichroism in Non-Chiral Nanostructures. *Nat. Commun.* **2014**, *5*, 4922.

(3) Liu, S.; Ni, J.; Zhang, C.; Wang, X.; Cao, Y.; Wang, D.; Ji, S.; Pan, D.; Li, R.; Wu, H.; Xin, C.; Li, J.; Hu, Y.; Li, G.; Wu, D.; Chu, J. Tailoring Optical Vortical Dichroism with Stereometamaterials. *Laser Photonics Rev.* **2022**, *16*, 2100518.

(4) Ni, J.; Liu, S.; Wu, D.; Lao, Z.; Wang, Z.; Huang, K.; Ji, S.; Li, J.; Huang, Z.; Xiong, Q.; Hu, Y.; Chu, J.; Qiu, C. W. Gigantic Vortical Differential Scattering as a Monochromatic Probe for Multiscale Chiral Structures. *Proc. Natl. Acad. Sci. U.S.A.* **2021**, *118*, e2020055118.

(5) Ni, J.; Liu, S.; Hu, G.; Hu, Y.; Lao, Z.; Li, J.; Zhang, Q.; Wu, D.; Dong, S.; Chu, J.; Qiu, C. W. Giant Helical Dichroism Of Single Chiral Nanostructures with Photonic Orbital Angular Momentum. *ACS Nano* **2021**, *15*, 2893−2900.

(6) Grier, D. G. A Revolution in Optical Manipulation. *Nature* **2003**, *424*, 810−816.

(7) Padgett, M.; Bowman, R. Tweezers with a Twist. *Nat. Photonics* **2011**, *5*, 343−348.

(8) Gecevičius, M.; Drevinskas, R.; Beresna, M.; Kazansky, P. G. Single Beam Optical Vortex Tweezers with Tunable Orbital Angular Momentum. *Appl. Phys. Lett.* **2014**, *104*, 231110.

(9) Wang, J.; Yang, J.-Y.; Fazal, I. M.; Ahmed, N.; Yan, Y.; Huang, H.; Ren, Y.; Yue, Y.; Dolinar, S.; Tur, M.; Willner, A. E. Terabit Free-Space Data Transmission Employing Orbital Angular Momentum Multiplexing. *Nat. Photonics* **2012**, *6*, 488−496.

(10) Bozinovic, N.; Yue, Y.; Ren, Y.; Tur, M.; Kristensen, P.; Huang, H.; Willner, A. E.; Ramachandran, S. Terabit-Scale Orbital Angular Momentum Mode Division Multiplexing in Fibers. *Science* **2013**, *340*, 1545−1548.

(11) Yan, Y.; Xie, G.; Lavery, M. P.; Huang, H.; Ahmed, N.; Bao, C.; Ren, Y.; Cao, Y.; Li, L.; Zhao, Z.; Molisch, A. F.; Tur, M.; Padgett, M. J.; Willner, A. E. High-Capacity Millimetre-Wave Communications with Orbital Angular Momentum Multiplexing. *Nat. Commun.* **2014**, *5*, 4876.

(12) Ren, H.; Briere, G.; Fang, X.; Ni, P.; Sawant, R.; Heron, S.; Chenot, S.; Vezian, S.; Damilano, B.; Brandli, V.; Maier, S. A.; Genevet, P. Metasurface Orbital Angular Momentum Holography. *Nat. Commun.* **2019**, *10*, 2986.

(13) Fang, X.; Ren, H.; Gu, M. Orbital Angular Momentum Holography for High-Security Encryption. *Nat. Photonics* **2020**, *14*, 102−108.

(14) Ren, H.; Fang, X.; Jang, J.; Burger, J.; Rho, J.; Maier, S. A. Complex-Amplitude Metasurface-Based Orbital Angular Momentum Holography in Momentum Space. *Nat. Nanotechnol.* **2020**, *15*, 948−955.

(15) Toyoda, K.; Miyamoto, K.; Aoki, N.; Morita, R.; Omatsu, T. Using Optical Vortex to Control the Chirality of Twisted Metal Nanostructures. *Nano Lett.* **2012**, *12*, 3645−3649.

(16) Ambrosio, A.; Marrucci, L.; Borbone, F.; Roviello, A.; Maddalena, P. Light-Induced Spiral Mass Transport in Azo-Polymer Films under Vortex-Beam Illumination. *Nat. Commun.* **2012**, *3*, 989.

(17) Ni, J.; Wang, C.; Zhang, C.; Hu, Y.; Yang, L.; Lao, Z.; Xu, B.; Li, J.; Wu, D.; Chu, J. Three-Dimensional Chiral Microstructures Fabricated by Structured Optical Vortices in Isotropic Material. *Light Sci. Appl.* **2017**, *6*, e17011.

(18) Pan, D.; Liu, S.; Li, J.; Ni, J.; Xin, C.; Ji, S.; Lao, Z.; Zhang, C.; Xu, B.; Li, R.; Fan, S.; Li, P.; Hu, Y.; Wu, D.; Chu, J. Rapid Fabrication of 3D Chiral Microstructures by Single Exposure of Interfered Femtosecond Vortex Beams and Capillary-Force-Assisted Self-Assembly. *Adv. Funct. Mater.* **2022**, *32*, 2106917.

(19) Cai, X.; Wang, J.; Strain, M. J.; Johnson-Morris, B.; Zhu, J.; Sorel, M.; O'Brien, J. L.; Thompson, M. G.; Yu, S. Integrated Compact Optical Vortex Beam Emitters. *Science* **2012**, *338*, 363−366.

(20) Miao, P.; Zhang, Z.; Sun, J.; Walasik, W.; Longhi, S.; Litchinitser, N. M.; Feng, L. Orbital Angular Momentum Microlaser. *Science* **2016**, *353*, 464−467.

(21) Li, H.; Phillips, D. B.; Wang, X.; Ho, Y.-L. D.; Chen, L.; Zhou, X.; Zhu, J.; Yu, S.; Cai, X. Orbital Angular Momentum Vertical-Cavity Surface-Emitting Lasers. *Optica* **2015**, *2*, 547.

(22) Sroor, H.; Huang, Y.-W.; Sephton, B.; Naidoo, D.; VallÉS, A.; Ginis, V.; Qiu, C.-W.; Ambrosio, A.; Capasso, F.; Forbes, A. High-Purity Orbital Angular Momentum States from a Visible Metasurface Laser. *Nat. Photonics* **2020**, *14*, 498−503.

(23) Yun, H.; Lee, S. Y.; Hong, K.; Yeom, J.; Lee, B. Plasmonic Cavity-Apertures As Dynamic Pixels for the Simultaneous Control of Colour and Intensity. *Nat. Commun.* **2015**, *6*, 7133.

(24) Karl, N. J.; Mckinney, R. W.; Monnai, Y.; Mendis, R.; Mittleman, D. M. Frequency-Division Multiplexing in the Terahertz Range Using a Leaky-Wave Antenna. *Nat. Photonics* **2015**, *9*, 717−720.

(25) Li, X.; Lan, T. H.; Tien, C. H.; Gu, M. Three-Dimensional Orientation-Unlimited Polarization Encryption by a Single Optically Configured Vectorial Beam. *Nat. Commun.* **2012**, *3*, 998.

(26) Lu, Y.; Zhao, J.; Zhang, R.; Liu, Y.; Liu, D.; Goldys, E. M.; Yang, X.; Xi, P.; Sunna, A.; Lu, J.; Shi, Y.; Leif, R. C.; Huo, Y.; Shen, J.; Piper, J. A.; Robinson, J. P.; Jin, D. Tunable Lifetime Multiplexing Using Luminescent Nanocrystals. *Nat. Photonics* **2014**, *8*, 32−36.

(27) Lei, T.; Zhang, M.; Li, Y.; Jia, P.; Liu, G. N.; Xu, X.; Li, Z.; Min, C.; Lin, J.; Yu, C.; Niu, H.; Yuan, X. Massive Individual Orbital

Angular Momentum Channels for Multiplexing Enabled by Dammann Gratings. *Light Sci. Appl.* **2015**, *4*, e257.
(28) Chen, S.; Xie, Z.; Ye, H.; Wang, X.; Guo, Z.; He, Y.; Li, Y.; Yuan, X.; Fan, D. Cylindrical Vector Beam Multiplexer/Demultiplexer Using Off-Axis Polarization Control. *Light Sci. Appl.* **2021**, *10*, 222.
(29) Ren, H.; Gu, M. Angular Momentum-Reversible Near-Unity Bisignate Circular Dichroism. *Laser Photonics Rev.* **2018**, *12*, 1700255.
(30) Ren, H.; Li, X.; Zhang, Q.; Gu, M. On-Chip Noninterference Angular Momentum Multiplexing Of Broadband Light. *Science* **2016**, *352*, 805−809.
(31) Yue, Z.; Ren, H.; Wei, S.; Lin, J.; Gu, M. Angular-Momentum Nanometrology in an Ultrathin Plasmonic Topological Insulator Film. *Nat. Commun.* **2018**, *9*, 4413.
(32) Genevet, P.; Lin, J.; Kats, M. A.; Capasso, F. Holographic Detection Of The Orbital Angular Momentum of Light with Plasmonic Photodiodes. *Nat. Commun.* **2012**, *3*, 1278.
(33) Chen, J.; Chen, X.; Li, T.; Zhu, S. On-Chip Detection of Orbital Angular Momentum Beam by Plasmonic Nanogratings. *Laser Photonics Rev.* **2018**, *12*, 1700331.
(34) Zhao, X.; Feng, X.; Liu, F.; Cui, K.; Zhang, W.; Huang, Y. A Compound Phase-Modulated Beam Splitter to Distinguish both Spin and Orbital Angular Momentum. *ACS Photonics* **2020**, *7*, 212−220.
(35) Feng, F.; Si, G.; Min, C.; Yuan, X.; Somekh, M. On-Chip Plasmonic Spin-Hall Nanograting for Simultaneously Detecting Phase and Polarization Singularities. *Light Sci. Appl.* **2020**, *9*, 95.
(36) Huang, C.; Zhang, C.; Xiao, S.; Wang, Y.; Fan, Y.; Liu, Y.; Zhang, N.; Qu, G.; Ji, H.; Han, J. Ultrafast control of vortex microlasers. *Science* **2020**, *367*, 1018−1021.
(37) Sun, W.; Liu, Y.; Qu, G.; Fan, Y.; Dai, W.; Wang, Y.; Song, Q.; Han, J.; Xiao, S. Lead halide perovskite vortex microlasers. *Nat. Commun.* **2020**, *11*, 4862.
(38) Cheng, J.; Sha, X.; Zhang, H.; Chen, Q.; Qu, G.; Song, Q.; Yu, S.; Xiao, S. Ultracompact orbital angular momentum sorter on a CMOS chip. *Nano Lett.* **2022**, *22*, 3993−3999.
(39) Zhang, H.; Sha, X.; Chen, Q.; Cheng, J.; Ji, Z.; Song, Q.; Yu, S.; Xiao, S. All-dielectric metasurface-enabled multiple vortex emissions. *Adv. Mater.* **2022**, *34*, 2109255.
(40) Lin, S. Y.; Fleming, J. G.; Hetherington, D. L.; Smith, B. K.; Biswas, R.; Ho, K. M.; Sigalas, M. M.; Zubrzycki, W.; Kurtz, S. R.; Bur, J. A Three-Dimensional Photonic Crystal Operating at Infrared Wavelengths. *Nature* **1998**, *394*, 251−253.
(41) Fleming, J. G.; Lin, S. Y.; El-Kady, I.; Biswas, R.; Ho, K. M. All-Metallic Three-Dimensional Photonic Crystals With A Large Infrared Bandgap. *Nature* **2002**, *417*, 52−55.
(42) Liu, N.; Guo, H.; Fu, L.; Kaiser, S.; Schweizer, H.; Giessen, H. Three-Dimensional Photonic Metamaterials at Optical Frequencies. *Nat. Mater.* **2008**, *7*, 31−37.
(43) Rill, M. S.; Plet, C.; Thiel, M.; Staude, I.; Von Freymann, G.; Linden, S.; Wegener, M. Photonic Metamaterials by Direct Laser Writing and Silver Chemical Vapour Deposition. *Nat. Mater.* **2008**, *7*, 543−546.
(44) Zhao, Y.; Belkin, M. A.; Alu, A. Twisted Optical Metamaterials for Planarized Ultrathin Broadband Circular Polarizers. *Nat. Commun.* **2012**, *3*, 870.
(45) Turner, M. D.; Saba, M.; Zhang, Q.; Cumming, B. P.; Schröder-Turk, G. E.; Gu, M. Miniature Chiral Beamsplitter Based on Gyroid Photonic Crystals. *Nat. Photonics* **2013**, *7*, 801−805.
(46) Kuzyk, A.; Schreiber, R.; Zhang, H.; Govorov, A. O.; Liedl, T.; Liu, N. Reconfigurable 3D Plasmonic Metamolecules. *Nat. Mater.* **2014**, *13*, 862−866.
(47) Woźniak, P.; De Leon, I.; Höflich, K.; Leuchs, G.; Banzer, P. Interaction of Light Carrying Orbital Angular Momentum with a Chiral Dipolar Scatterer. *Optica* **2019**, *6*, 961.
(48) Brullot, W.; Vanbel, M. K.; Swusten, T.; Verbiest, T. Resolving Enantiomers Using the Optical Angular Momentum of Twisted Light. *Sci. Adv.* **2016**, *2*, e1501349.
(49) Ouyang, X.; Xu, Y.; Xian, M.; Feng, Z.; Zhu, L.; Cao, Y.; Lan, S.; Guan, B.-O.; Qiu, C.-W.; Gu, M. Synthetic helical dichroism for six-dimensional optical orbital angular momentum multiplexing. *Nat. Photonics* **2021**, *15*, 901−907.
(50) Zhang, Z.; Qiao, X.; Midya, B.; Liu, K.; Sun, J.; Wu, T.; Liu, W.; Agarwal, R.; Jornet, J. M.; Longhi, S. Tunable topological charge vortex microlaser. *Science* **2020**, *368*, 760−763.
(51) Cai, X.; Wang, J.; Strain, M. J.; Johnson-Morris, B.; Zhu, J.; Sorel, M.; O'Brien, J. L.; Thompson, M. G.; Yu, S. Integrated compact optical vortex beam emitters. *Science* **2012**, *338*, 363−366.

https://doi.org/10.1021/acs.nanolett.2c04860
Nano Lett. 2023, 23, 2304−2311